Quantum Sensing and Information Processing

Lecture 8: Error Modelling –The Impact of Noise on Quantum Devices

September 26th, 2019

Stephen B. Libby
Theory and Modeling Group Leader
Physics Division
Physical and Life Sciences

LLNL-PRES-794638
This work was performed under the auspices of the U.S. Department of Energy by Lawrence Livermore National Laboratory under contract DE-AC52-07NA27344. Lawrence Livermore National Security, LLC

Lawrence Livermore National Laboratory

Special thanks to:

- Admins: Tonya Dye, Shane Athey (ENG), Alyssa Lee (COMP)
- Video: Bob Sickles, Dave Hopkins, Cheryl Hernandez, Cheryl Nunez, Matt Story, Lauren Bouthillier and Don Harrison
- Derivative Classifiers and Directorate Reviewers: Scott Kohn, Everett Wheelock, Simon Labov, Steve Kreek, Amy Waters, Edna Didwall and Jeff Stevens
- Web Master: Stacy Peterson, Pam Williams
- LLNL Public Affairs office: Jeremy Thomas and Madeline Burchard
- Lecturers: Jonathan Dubois, Steve Libby, Dave Chambers, Andreas Baertschi, Matt Horsley
- Advanced Simulation and Computing Program (LANL) and the Center for Applied Scientific Computing (LLNL).
- ENG DAD S&T: Rob Sharpe

https://casis.llnl.gov/seminars/quantum_information

‘Noisy’ errors in quantum sensors & computers drive design innovations to minimize their impact.

- Threshold theorem, quantum error correction, fault tolerance
- Quantification of quantum noise processes and their impact:
  - Ramsey Interferometry Noise – quantum projection & the ‘standard quantum limit’
  - Allan deviation
  - Example: Noise interacting with differing quantum correlation – e.g. squeezing
  - Quantum process tomography / Randomized benchmarking
- Microscopic models of noise processes – Hamiltonians for gate and sensor physics.
  - Control, ‘SPAM,’ and intrinsic (quantum, thermal etc.) noise.
  - Interesting computational challenges often go hand and hand with accurate assessment of noise impacts.
- Noise mitigation for different gate schemes
  - dynamical decoupling, and Molmer-Sorensen gate vs. polychromatic gates with intrinsic dynamical decoupling.
- Case study 1 – Atom interferometry for gravity/gyroscopic sensing.
- Case study 2 – Ion trap quantum computing (physics error budget,

Quantum Sensing: Detection, Interferometry, Noise* - *Requirements*!

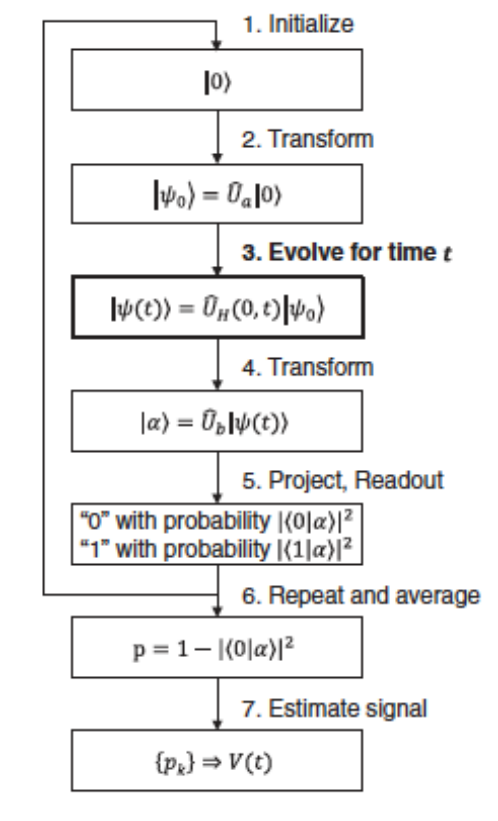

Basic steps in the quantum sensing process

How does quantum noise limited sensitivity drive our 'quantum device' design?

Atomic fountain clock & cold atom interferometry examples, as well as phase detection for quantum computing alfgorithms (e.g. Shor).

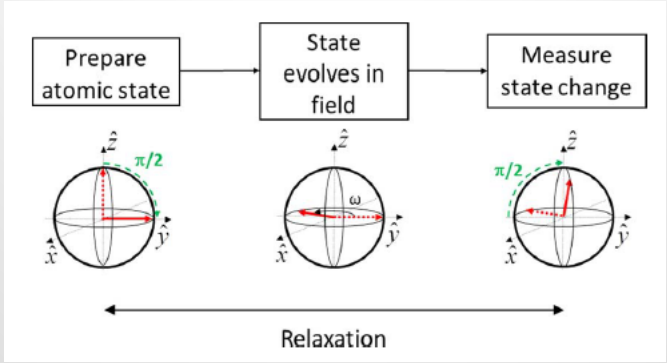

Ramsey Interferometry

$$|\psi_0\rangle = |+\rangle \equiv \frac{1}{\sqrt{2}}(|0\rangle + |1\rangle) \Rightarrow |\psi(t)\rangle = \frac{1}{\sqrt{2}}(|0\rangle + e^{-i\omega_0 t}|1\rangle) \Rightarrow |\alpha\rangle = \tfrac{1}{2}(1 + e^{-i\omega_0 t})|0\rangle + \tfrac{1}{2}(1 - e^{-i\omega_0 t})|1\rangle$$

$$p = 1 - |\langle 0|\alpha\rangle|^2 = \sin^2(\omega_0 t/2) = \tfrac{1}{2}[1 - \cos(\omega_0 t)]$$

$$\hat{H}_{V_\perp} = \frac{1}{2}\gamma V_\perp \sigma_x = \omega_1 \sigma_x$$

Quantum Projection Noise Limited Sensitivity

$$\delta F_{\min} = \frac{h\delta\varphi}{\mu T}$$

$$\delta F_{\min} = \frac{h\delta\varphi}{\mu T_2}\sqrt{\frac{T_2}{T}} = \frac{h}{\mu\sqrt{T_2 T N}}$$

**Quantum sensing*, C. L. Degen, F. Reinhard, P. Cappellaro, RMP, 89, 035002, (2017).

Atomic Sensors – a review, J. Kitching, S. Knappe, E. A. Donley, IEEE Sensors, 11, 9, 1749, (2011).

Squeezed atomic states and projection noise in spectroscopy, D. J. Wineland, J. J. Bollinger, W. M. Itano, and D. J. Heinzen, Phys. Rev. A, vol. 50, pp. 67–88, (1994).

Quantum Projection Noise and the Standard Quantum Limit

- Perturb around Rabi frequency
- Slope and variance detection
- N copies of quantum system $p = \frac{N_1}{N}$
- Uncertainty in p:

$$\sigma^2_{p,\text{quantum}} = \frac{1}{N} p(1-p)$$

- Projective readout noise:

$$\sigma^2_{p,\text{quantum}} = \frac{1}{4N} \quad \text{for } p_0 = 0.5$$

$$\text{SNR} = \frac{\delta p_{\text{obs}}}{\sigma_p} = \delta p(t) e^{-\chi(t)} 2C\sqrt{N}$$

- Pure state (non-squeezed) get standard quantum limit (quantum Cramer-Rao bound)

$$\Delta V_N \geq \frac{1}{2\gamma\sqrt{N}\Delta H}$$

$$\Delta H := \sqrt{\langle H^2 \rangle - \langle H \rangle^2}$$

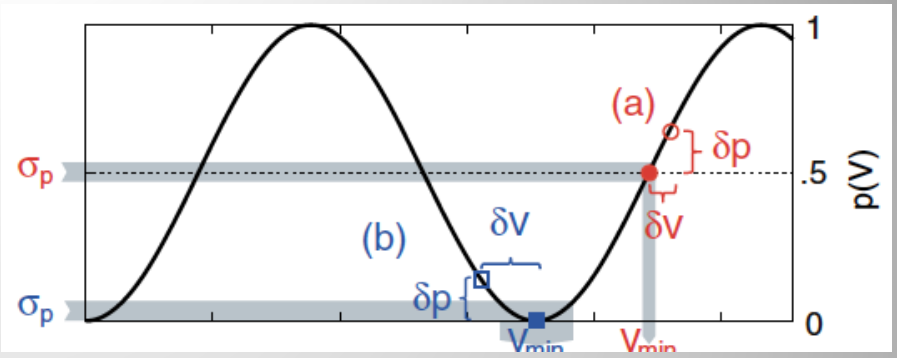

$$\hat{H}_{V_\perp} = \tfrac{1}{2}\gamma V_\perp \sigma_x = \omega_1 \sigma_x$$

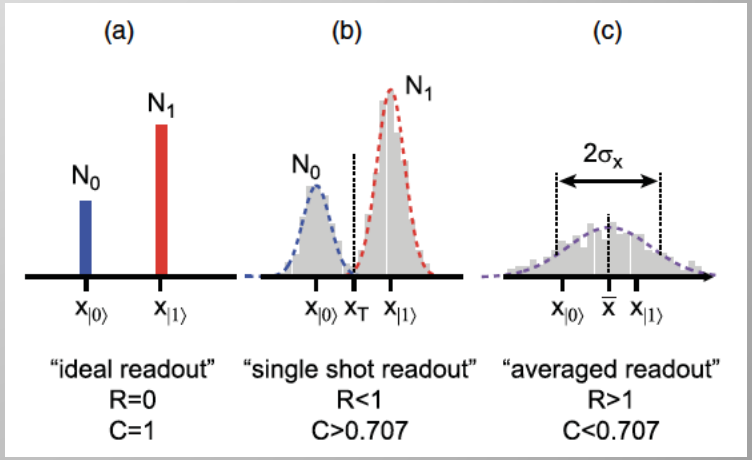

What can we learn from the Allan variance?

$$\sigma_X^2(\tau) = \frac{1}{2(N-1)t_s^2}\sum_{j=1}^{N-1}(x_{j+1}-x_j)^2$$

$$\sigma_X^2(mt_s) = \frac{1}{2(N-2m)m^2t_s^2}\sum_{j=1}^{N-2m}(x_{j+m}-x_j)^2$$

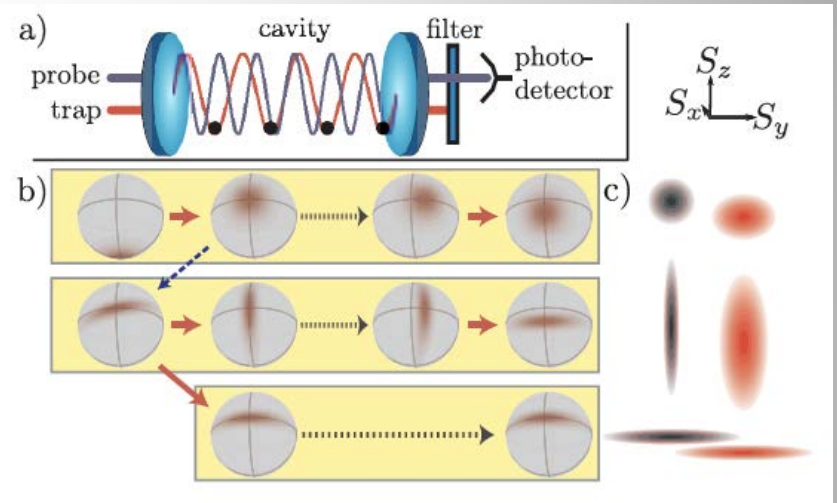

- Allan variance formulae for sequential measurements and groupings (above)
- Leroux et. al. – PRL 104, 2010 (spin squeezed states improving atomic clock precision (right).
- Setup a)- ^{87}Rb atoms in optical resonator.
- Pulse sequences b) Standard Ramsey, add (blue arrow) squeezing.
- Impact of phase fluctuation noise c)
- Allan Deviation comparison of squeezed spin performance vs. SQL. $1.85 \times 10^{-9}\ \mathrm{s}^{1/2}/\sqrt{\tau}$

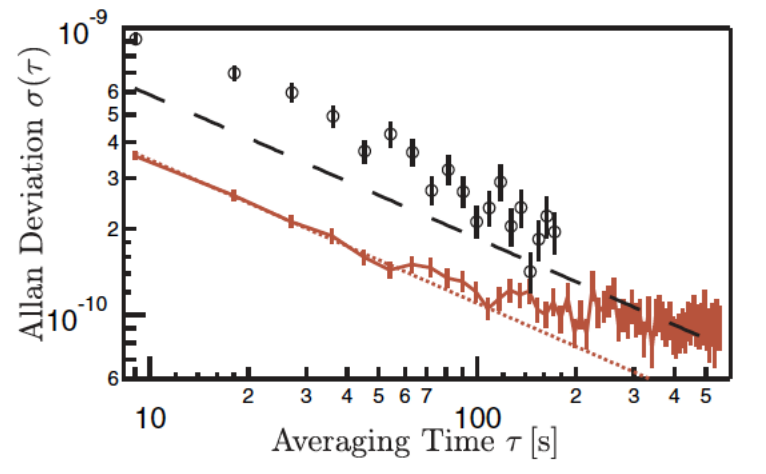

Quantum Process Tomography

- χ_{ab} - 4^n x 4^n 'process' matrix for n qubits.
- 2 qubit case – input states: direct product of Pauli matrix eigenvectors.
- A_a complete set of operators
- *Quantum process tomography of a Molmer-Sorensen interaction,* Navon et. al., PRA 90, 2014
- *Compare with more 'economical' noise tests – e.g. randomized benchmarking – (direct products of Clifford operators with random unitary insertions).*
- *What does randomized benchmarking miss?*
- *24 single qubit Cliffords, 720 two qubit Cliffords, etc.*

$$\mathcal{E}[\rho] = \sum_{a,b} \chi_{ab} A_a \rho A_b^\dagger$$

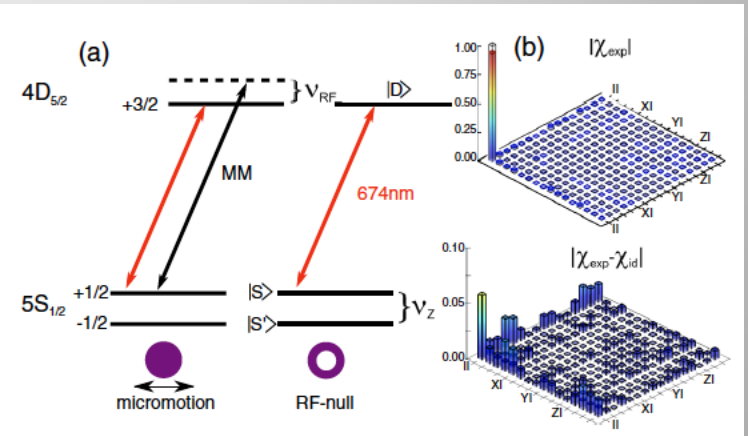

- $^{88}Sr^+$ ion optical qubit
- Test of identity operation map
- Maximum likelihood detection with physical constraint

Case Study 1: Atom Interferometry

- Laser pulses act as beam splitters and mirrors for the atomic wavefunction
- Highly sensitive to accelerations (e.g. gravity…)

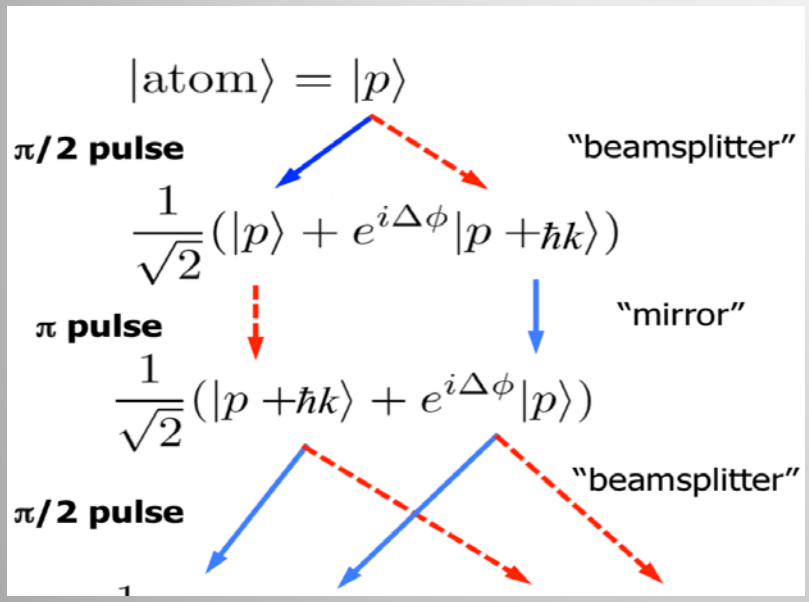

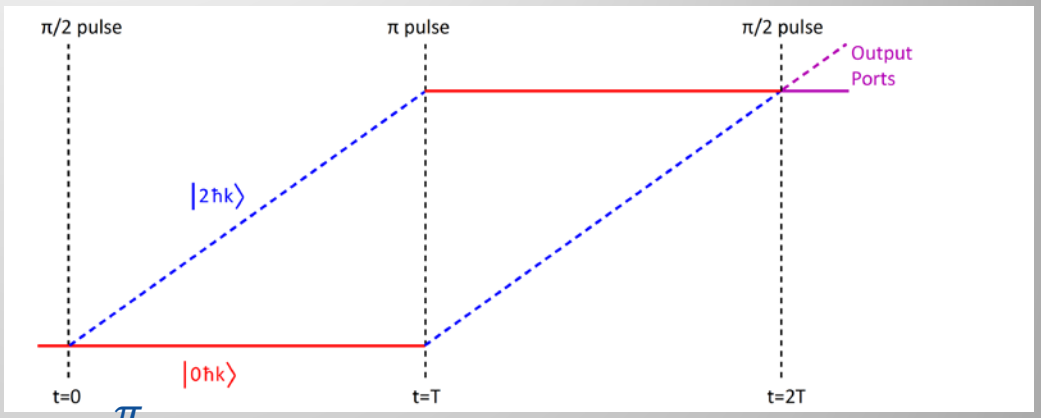

$$\frac{1}{2}((1 + e^{i\Delta\phi})|p\rangle + ((1 - e^{i\Delta\phi}))|p + \hbar k\rangle)$$

$$\text{Probability in State } |p\rangle = \cos^2\left(\frac{\Delta\phi}{2}\right)$$

$$\text{Probability in State } |p + \hbar k\rangle = \sin^2\left(\frac{\Delta\phi}{2}\right)$$

π

Effects scale like AREA, so

Long T good

High momentum good

Note the key role of a Hahn-like π pulse.

Cold-Atom interferometry gravity sensors demonstrate off-the-chart performance

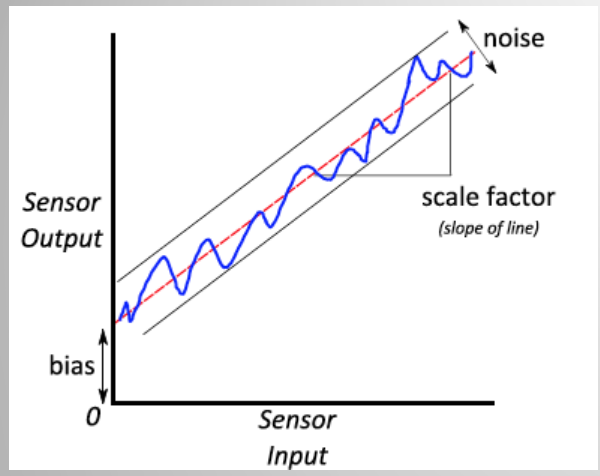

AI sensor performance in open literature:

- Bias stability: <<10^{-10} g
- Noise: < 4×10^{-9} g/Hz$^{1/2}$
- Scale Factor: < 10^{-10}

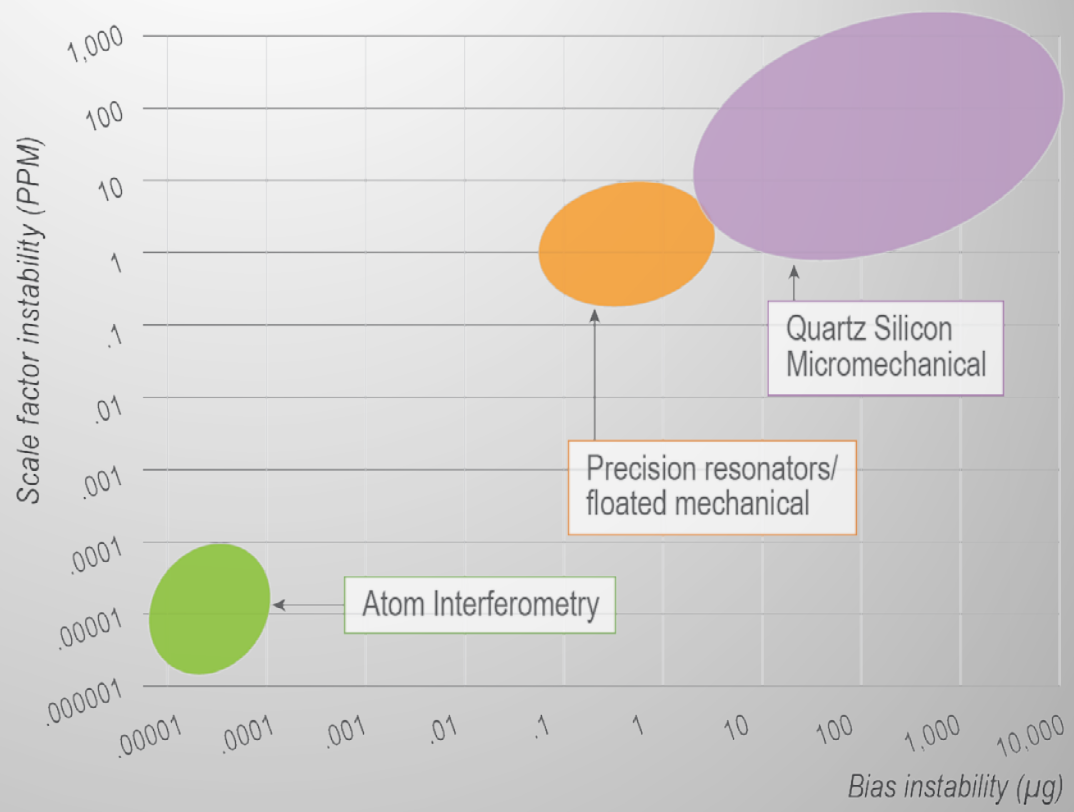

Quantum projection noise limited performance (present) depends on *D, T,* number of atoms *N*, photon recoil k_{eff}, interference fringe contrast η:

$$\Delta T_{zz} \approx \frac{1}{\eta\sqrt{N}\, D\, k_{eff} T^2}$$

Squeezed state detection ~ $1/N^q$ (.5 < q < 1). Uncertainty limit ~ 1/N

(Light-pulse) atom interferometry builds on laser cooled atoms ($T \leq 10^{-6}$ K)

Resonant optical interaction

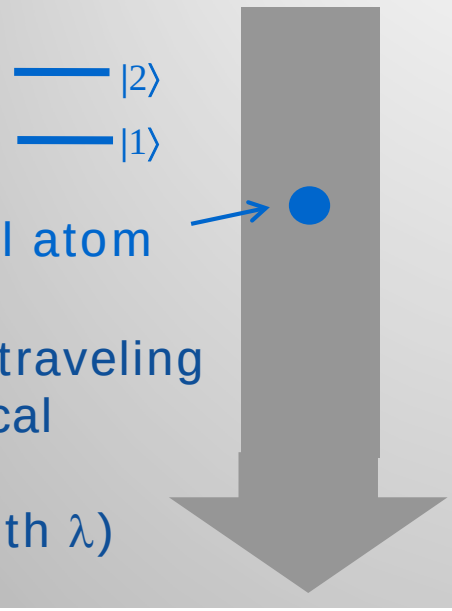

$$|\psi(t)\rangle = \cos\left(\frac{\Omega t}{2}\right)|1,\mathbf{p}\rangle + e^{-i\frac{\pi}{2}}e^{i\phi_L}\sin\left(\frac{\Omega t}{2}\right)|2,\mathbf{p}+\hbar\mathbf{k}_{\mathrm{eff}}\rangle$$

- Errors include: motion during laser pulses, light shift, quantum corrections, laser wavefront, phase error…

Recoil diagram

- Momentum conservation between atom and laser light field (recoil) leads to spatial separation of atomic wavepackets.

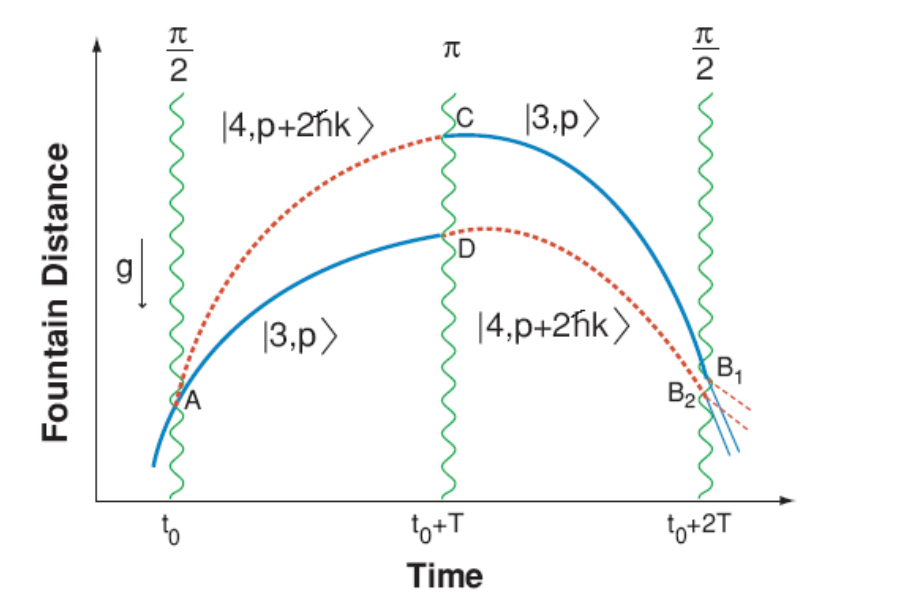

$$\phi_{tm} = \vec{k}_{eff}\delta\vec{\phi},$$
$$\delta\vec{\phi} = \delta\vec{x}(t_1+2T) - 2\delta\vec{x}(t_1+T) + \delta\vec{x}(t_1)$$

$$\delta\vec{x}(t) = \int_0^t dt'\,(t-t')\,\delta\vec{g}\left[\vec{x}_0(t')\right]$$

Ion traps: implementing controlled quantum logic

- Divincenzo quantum computing criteria met:
  - Scalable, well characterized qubits (e.g. ion hyperfine states in Wineland $^{9}Be^{+}$ scheme).
  - Ability to initialize to $|0000..\rangle$
  - Long decoherence time.
  - Universal gate set.
  - Qubit specific, quantum efficient measurement capability.
  - *Noise affects ALL of these criteria*!

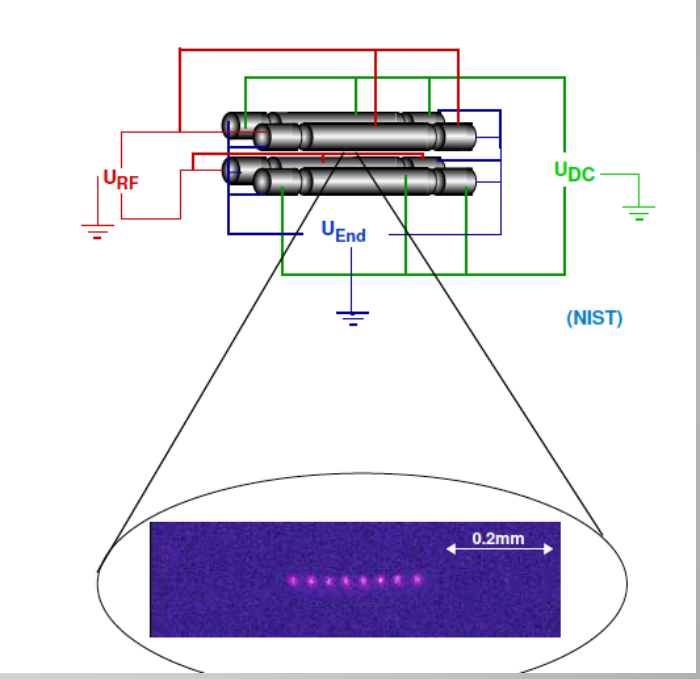

- Energy scales: ω_{recoil} ~ 50 - 250 kHz, ω_{axial} ~ 2-10 MHz, Ω_{Rabi} ~ .1 to 10 MHz, $\omega_{hyperfine}$ ~ 1.25 GHz ($^{9}Be^{+}$ S state), $\omega_{optical}$ ~ 729 nm ($^{40}Ca^{+}$)

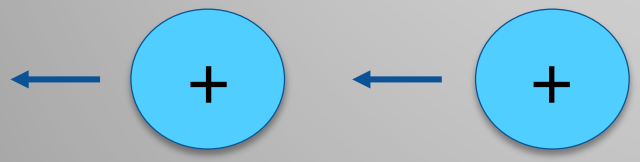

Laser Gradient: $\propto \eta\Omega$

$$\eta = k_z(\sqrt{\hbar / 2m\omega}) < 1$$

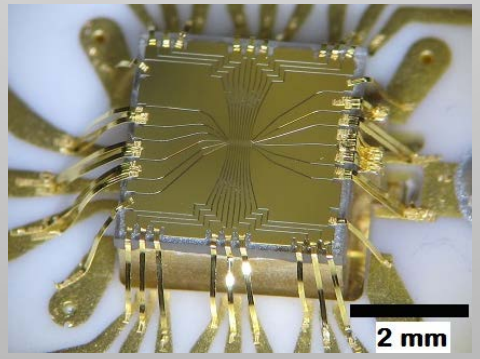

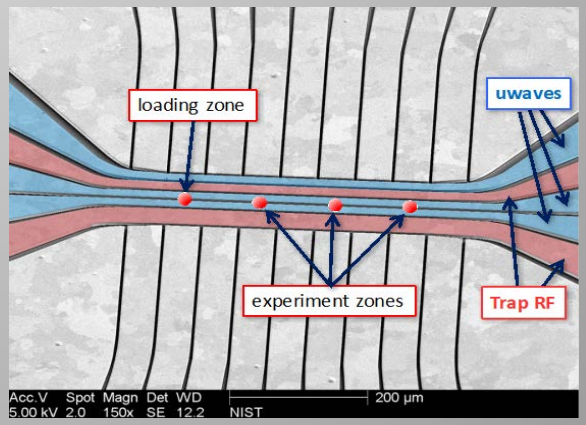

Ion trap quantum dynamics – effective Hamiltonians

$$H(t) = \overbrace{\underbrace{\frac{p^2}{2m} + \frac{m}{2}\omega_t^2 x^2}_{\text{harmonic oscillator}} + \underbrace{\frac{1}{2}\hbar\omega_a\sigma_z}_{\text{spin part}}}^{H_0} + \overbrace{\underbrace{\frac{1}{2}\hbar\Omega\left(\sigma^+ + \sigma^-\right)\left(e^{i(kx-\omega_l t+\phi)} + e^{-i(kx-\omega_l t+\phi)}\right)}_{\text{laser-ion interaction}}}^{H_1}$$

$$H = H_0 + H_{\text{int}}$$

$$H_0 = \nu(a^\dagger a + 1/2) + \omega_{eg}\sum_j \sigma_{zj}/2$$

$$H_{\text{int}} = \sum_j \frac{\Omega_j}{2}(\sigma_{+j}\ e^{i(\eta(a+a^\dagger)-\omega_j t)} + h.c.),$$

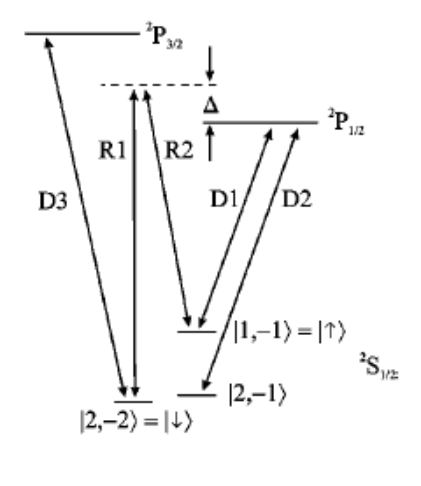

- Ion cooling analogous to neutral cold atoms –here Doppler cooling followed by 'phonon sideband' cooling.
- Wineland et. al. hyperfine qubit in $^9Be^+$ analogous to neutral alkali (Cs or Rb) ground state hyperfine dynamics.
- Blatt et. al. scheme in $^{40}Ca^+$ - qubit is on quadrupole transition.

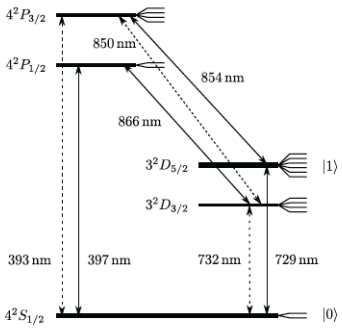

Figure 3.2 – *Atomic energy levels of $^{40}Ca^+$ with Zeeman substructure. The transitions indicated by solid arrows are driven by laser radiation during the experiment. The levels $S_{1/2}$ and $D_{5/2}$ are associated with the logical states $|0\rangle$ and $|1\rangle$. We use the standard atomic level notation $n^{2S+1}L_J$, where n is the principal quantum number, S is the spin angular momentum, L is the orbital angular momentum and J is the total angular momentum.*

Case study 2 A: Ion trap quantum processing
2 Qubit Gates with $^{43}Ca^{+}$ - Oxford (Ballance 2014)

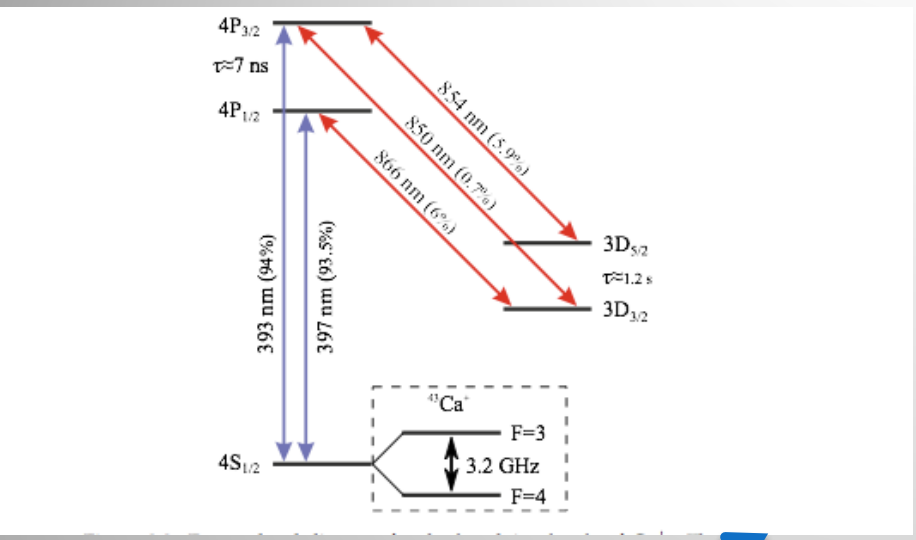

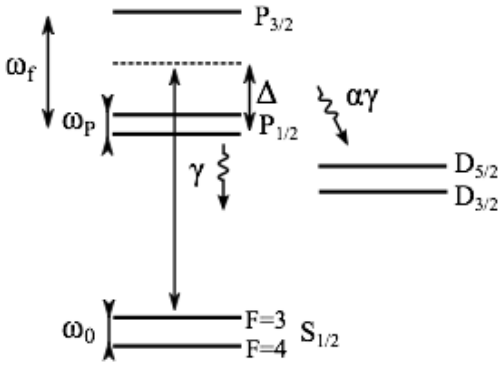

Figure 3.2: Simplified level scheme of $^{43}Ca^{+}$. The Raman beams address the S-P transition. The P states decay mostly back to S, at rate $\gamma = 132 \times 10^{6}\,s^{-1}$, and occasionally into D at rate $\alpha\gamma$ ($\alpha \approx 0.06$). The hyperfine splittings are shown for the $S_{1/2}$ and $P_{1/2}$ levels only.

- $^{43}Ca^{+}$ Grotrian diagram, hyperfine 'stretch' qubit and Raman laser drive scheme.

- Gate experimental sequence for creating a Bell state.

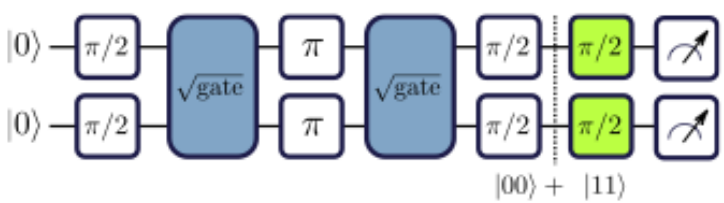

Figure 8.2: The gate experiment sequence. The two light-shift gate pulses (blue boxes) are inserted in the arms of a spin-echo (white boxes). The π- and $\pi/2$-pulses are driven by microwaves. At the end of the spin-echo sequence a Bell state is produced (dotted vertical line). We either directly measure this Bell state, or apply a further 'analysis' $\pi/2$-pulse with a variable phase (green boxes).

$$\mathcal{H} = \sum_j \frac{i\eta_c}{2} \left(\Omega_\uparrow |\uparrow_j\rangle\langle\uparrow_j| - \Omega_\downarrow |\downarrow_j\rangle\langle\downarrow_j|\right) e^{-i\delta t} e^{i\phi_0} e^{i\Delta k z_j^0} a_c^\dagger + \text{h.c.}$$

C. Ballance et. al. arXiv 1406.5473v1, 2014 – two qubit gate interaction – Bell state fidelity test

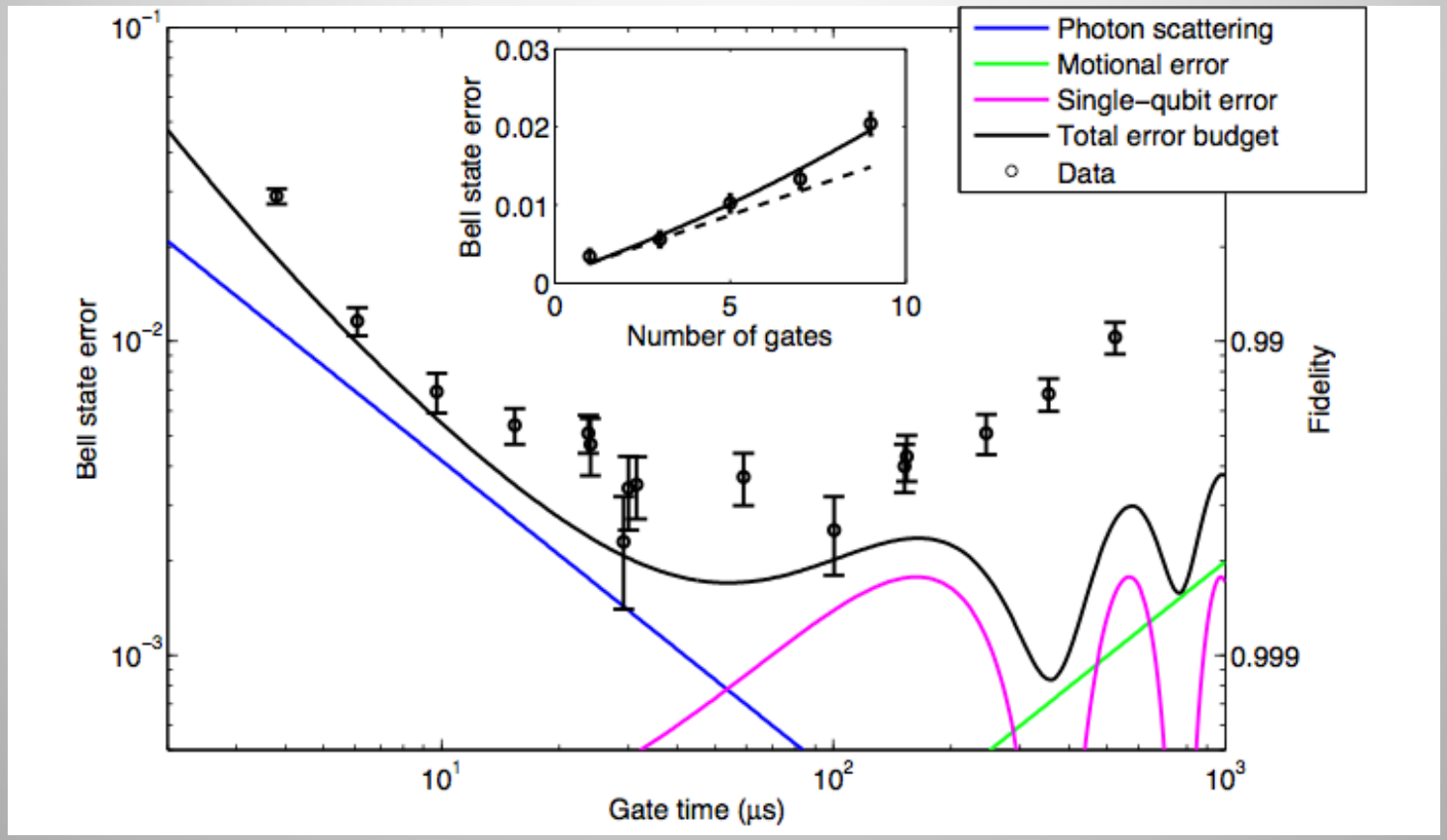

- We are interested in understanding how multiple physical error mechanisms constrain gate times with 'good' coherence.

Gate error rates as a function of Raman drive detuning

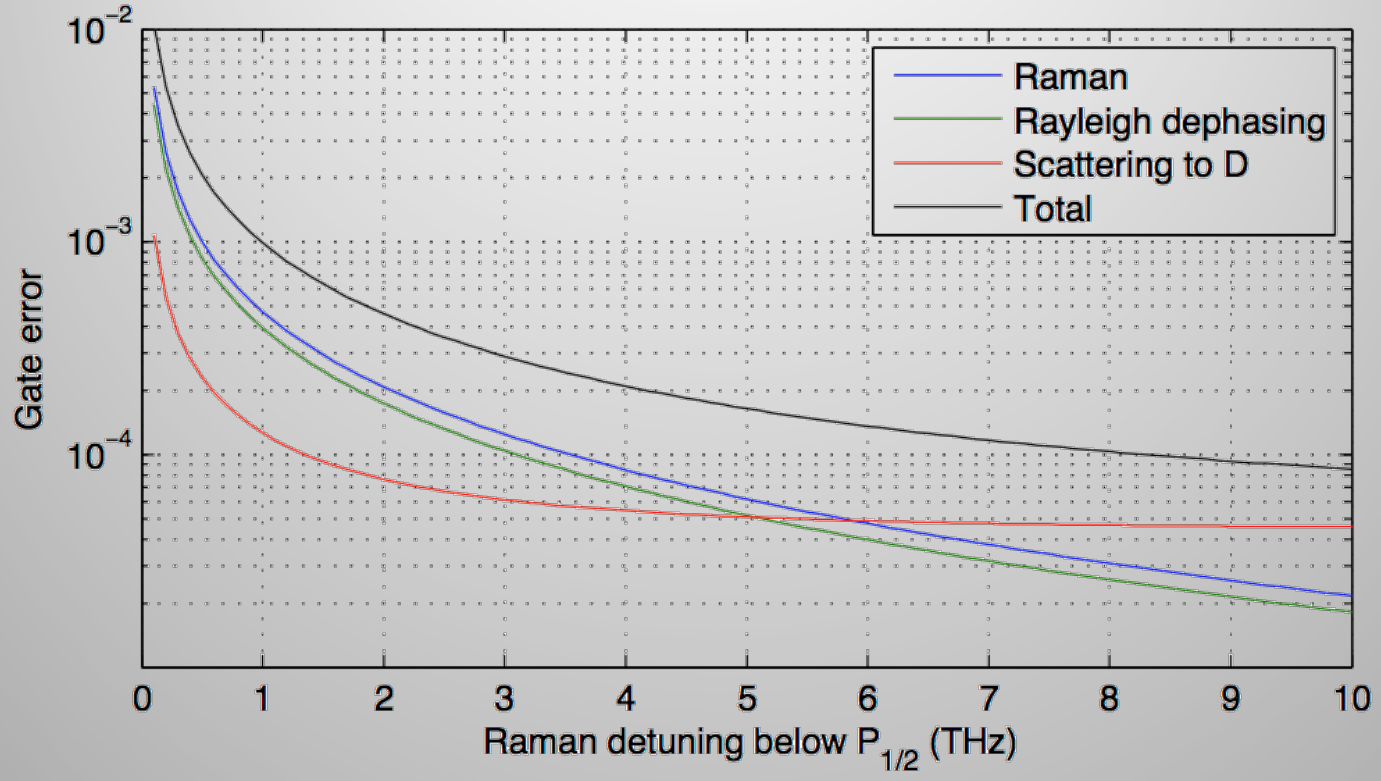

C. Ballance experiment, error budget

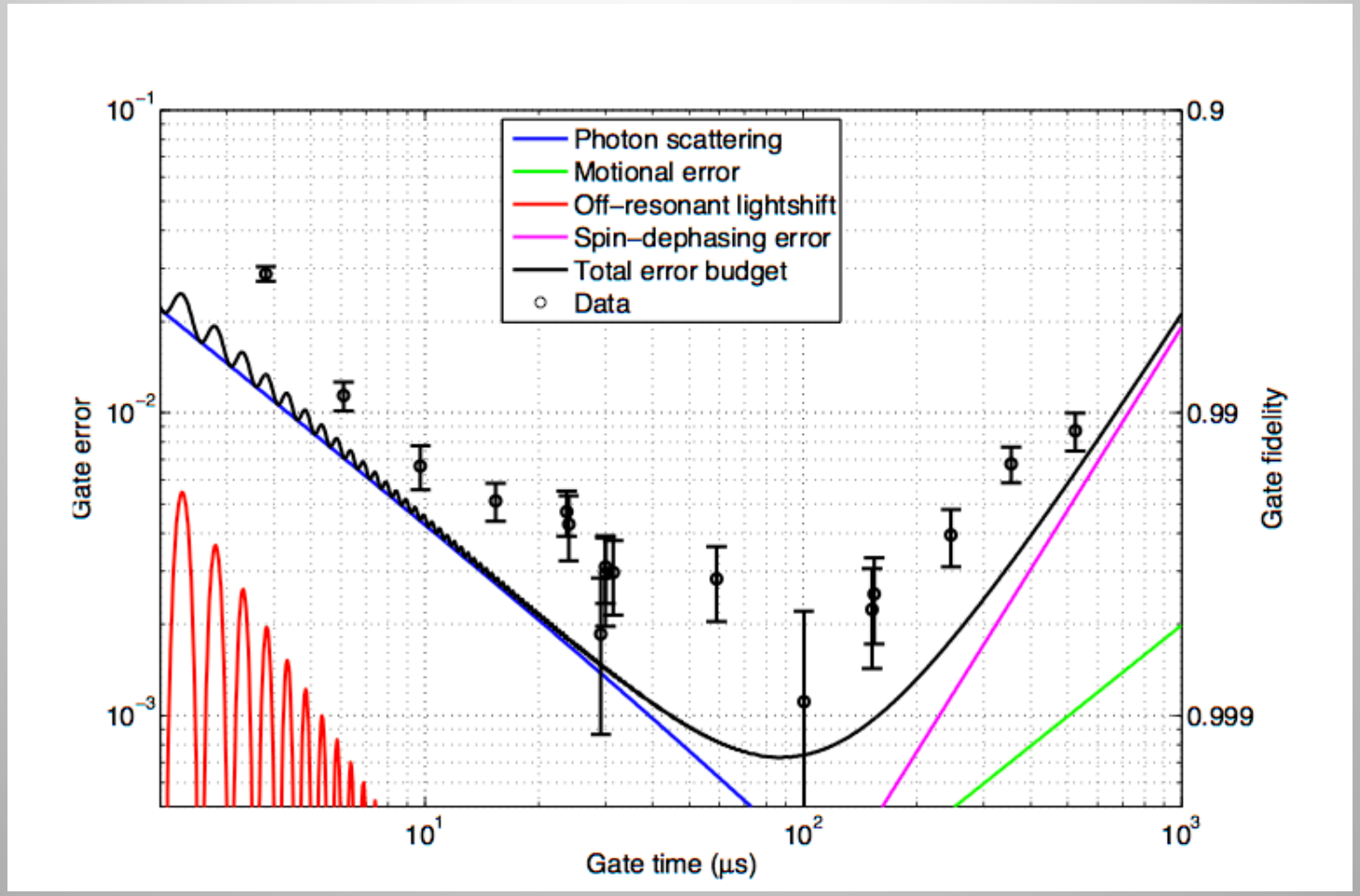

C. Ballance thesis fig 8.13

Jonathan Dubois's multiphysics error fit to Ballance data

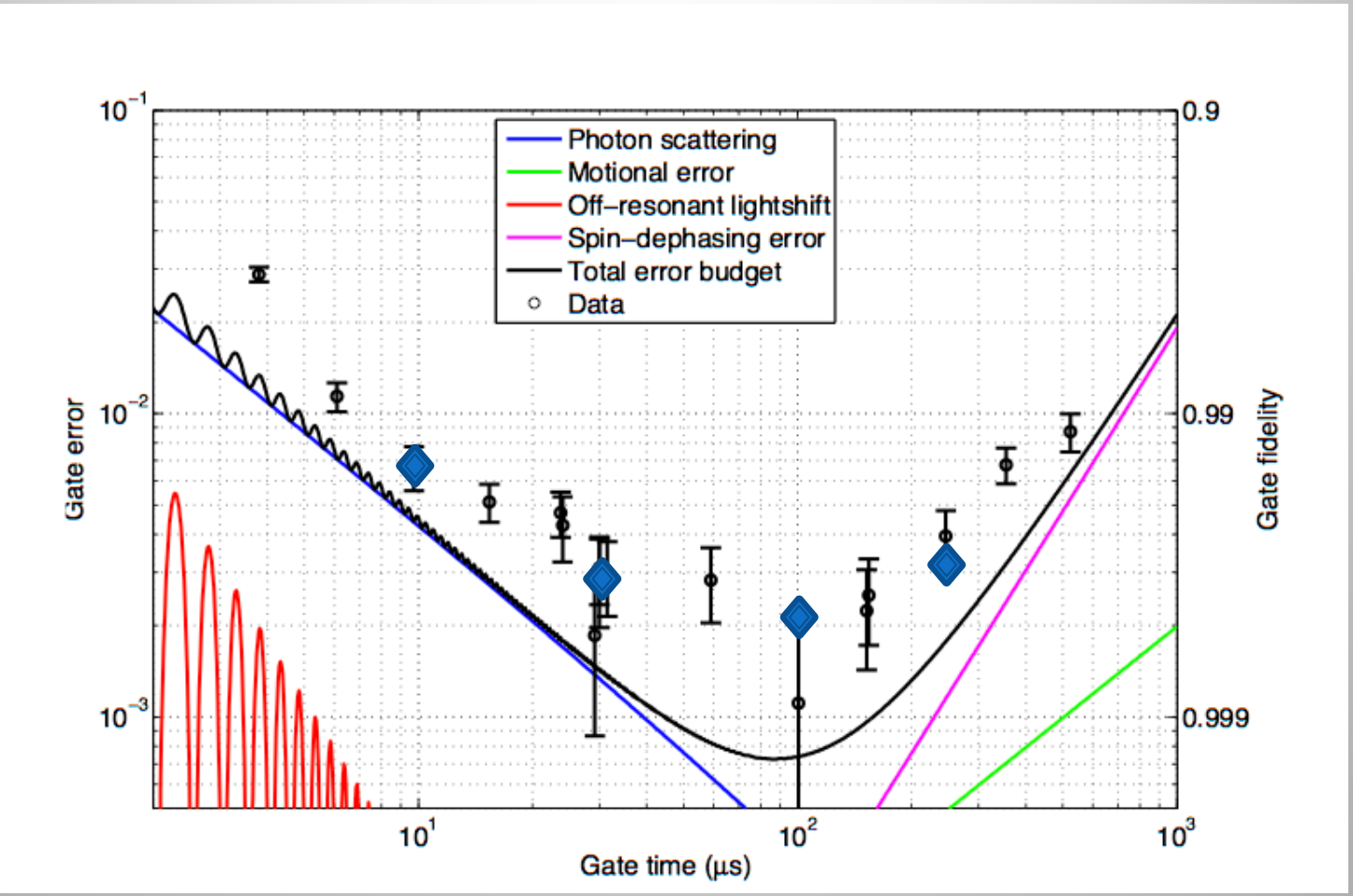

C. Ballance thesis fig 8.13

Case study 2B - 'magtrap,' laser-free gates have no appreciable photon scattering error – potentially big impact on accuracy and speed.

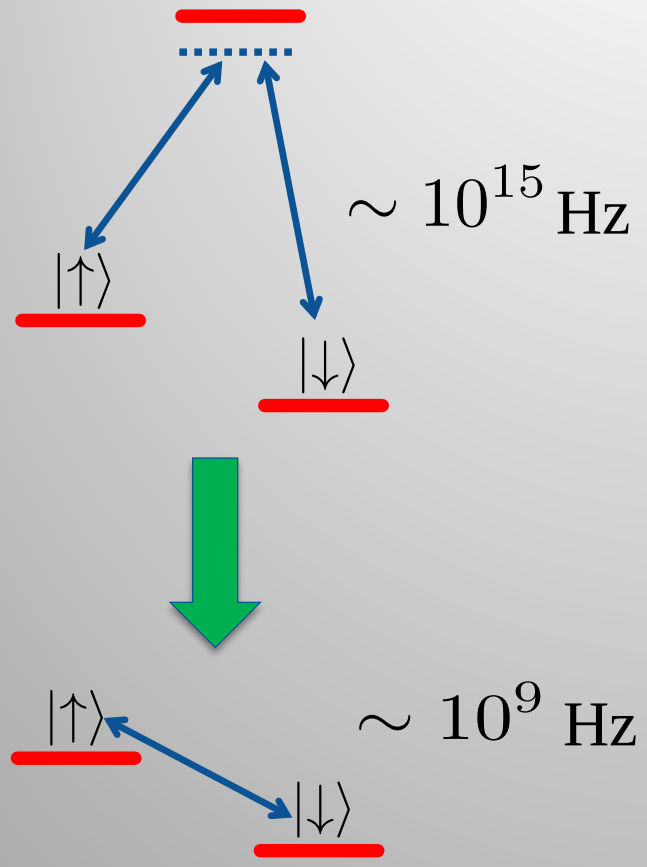

Advantages to laser-free:

- No photon scattering
- Only low-power cooling lasers
- Easier phase control

Disadvantages to laser-free:

- Slower

Bigger impacts from:

- qubit frequency shifts
- motional decoherence

Goals:

- Reduce sensitivity to noise
- Reduce experimental overhead

Qubit frequency shifts

ZZ Gate:

$$\hat{H}(t) = \hbar\Omega\hat{\sigma}_z\left(\hat{a}e^{-i\delta t} + \hat{a}^\dagger e^{i\delta t}\right) + \frac{\hbar\Delta'}{2}\hat{\sigma}_z$$

- Gate commutes with qubit frequency shift
  - Static shifts removed with simple spin-echo

- On-resonant E-field ⟶ technically challenging

Dynamically-decoupled MS Gate:

$$\hat{H}(t) = \hbar\Omega\hat{\sigma}_x\left(\hat{a}e^{-i\delta t} + \hat{a}^\dagger e^{i\delta t}\right) + \frac{\hbar\Delta'}{2}\hat{\sigma}_z + \frac{1}{2}\hbar\Omega_{dd}\hat{\sigma}_x$$

- Significant experimental overhead

PRL **117,** 140501 (2016)

‘Laser-free’ gates

$$\hat{H}(t) = 2\hbar\Omega_\mu \cos(\delta t)\hat{\sigma}_i + 2\hbar\Omega_g f(t)\hat{\sigma}_j\left\{\hat{a}e^{-i\omega_r t} + \hat{a}^\dagger e^{i\omega_r t}\right\}$$

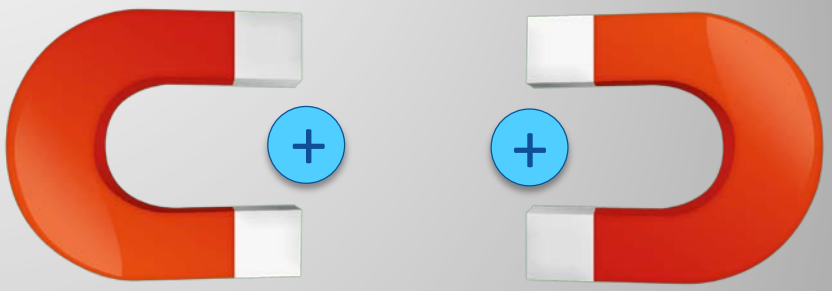

Static frequency gradient:

$f(t) = 1$

PRL **117,** 220501 (2016)

Near-qubit frequency gradient:

$f(t) = \cos([\omega_0 + \omega]t) + \cos([\omega_0 - \omega]t)$

PRL **101,** 090502 (2008)
Nature **476,** 181 (2011)
PRL **117,** 220501 (2016)
arXiv:1902.07028

$\omega_0 \equiv$ qubit frequency

$\omega \sim \omega_r$

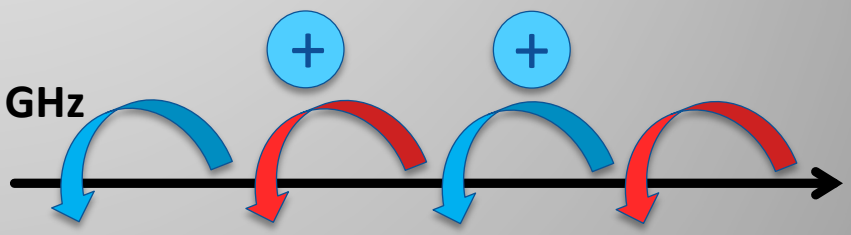

Near-motional frequency gradient:

$f(t) = \cos(\omega_g t)$ $\omega_g \sim \omega_r$

PRL **122,** 163201 (2019)

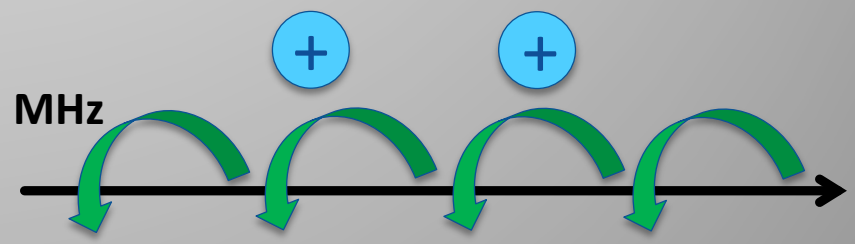

Bichromatic Interaction Picture Gates

$$\hat{\sigma}_i \rightarrow \hat{\sigma}_z$$
$$\hat{\sigma}_j \rightarrow \hat{\sigma}_z$$
$$f(t) \rightarrow \cos(\omega_g t)$$

Near-motional gradient:

$$\hat{H}_I(t) = 2\hbar\Omega_g \cos(\omega_g t)\left\{\hat{a}e^{-i\omega_r t} + \hat{a}^\dagger e^{i\omega_r t}\right\}\left\{\hat{\sigma}_z\left[J_0\left(\frac{4\Omega_\mu}{\delta}\right) + 2\sum_n J_{2n}\left(\frac{4\Omega_\mu}{\delta}\right)\cos(2\delta t)\right] + 2\hat{\sigma}_y \sum_n J_{2n-1}\left(\frac{4\Omega_\mu}{\delta}\right)\sin([2n-1]\delta t)\right\}$$

Even resonances:

$$2\delta \sim \omega_r - \omega_g \text{ ——— } \hat{H}_I \simeq \hbar\Omega_g J_2\left(\frac{4\Omega_\mu}{\delta}\right)\hat{\sigma}_z\left\{\hat{a}e^{i\Delta t} + \hat{a}^\dagger e^{-i\Delta t}\right\}$$

Odd resonances:

$$\delta \sim \omega_r - \omega_g \text{ ——— } \hat{H}_I \simeq i\hbar\Omega_g J_1\left(\frac{4\Omega_\mu}{\delta}\right)\hat{\sigma}_y\left\{\hat{a}^\dagger e^{-i\Delta t} - \hat{a}e^{i\Delta t}\right\}$$

NJP **10,** 013003 (2008) NJP **21,** 033033 (2019)

*Intrinsic Dynamical Decoupling (IDD) – R. T. Sutherland

Effective Shift:

$$\frac{\hbar\Delta'}{2}\hat{\sigma}_z \rightsquigarrow J_0\left(\frac{4\Omega_\mu}{\delta}\right)\frac{\hbar\Delta'}{2}\hat{\sigma}_z$$

Tuning:

$$\delta \sim \omega_r - \omega_g$$

$$2\delta \sim \omega_r - \omega_g$$

Gate speed:

$$\propto J_1\left(\frac{4\Omega_\mu}{\delta}\right)$$ **MS gate**

$$\propto J_2\left(\frac{4\Omega_\mu}{\delta}\right)$$ **ZZ gate**

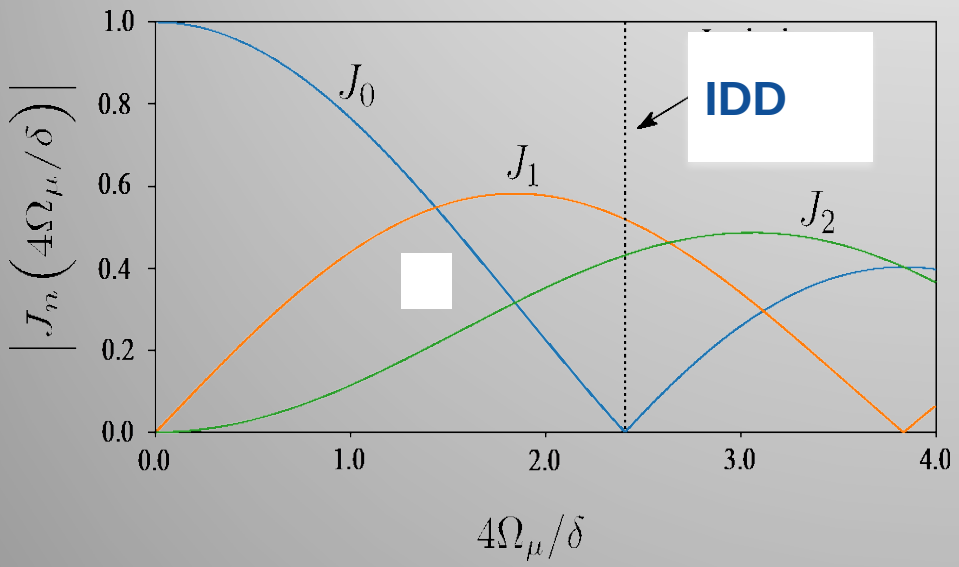

Experimentally demonstrated

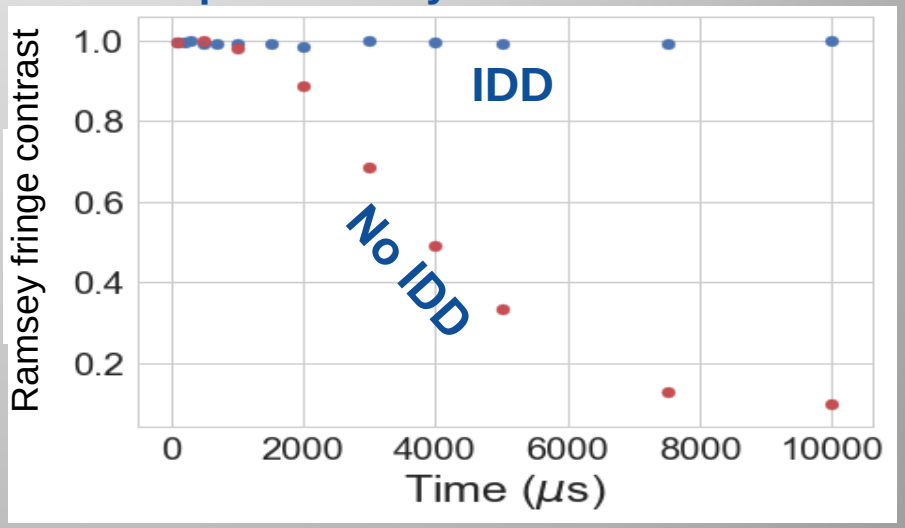

*NJP **21,** 033033 (2019)

Intuitive explanation of why intrinsic dynamical decoupling works

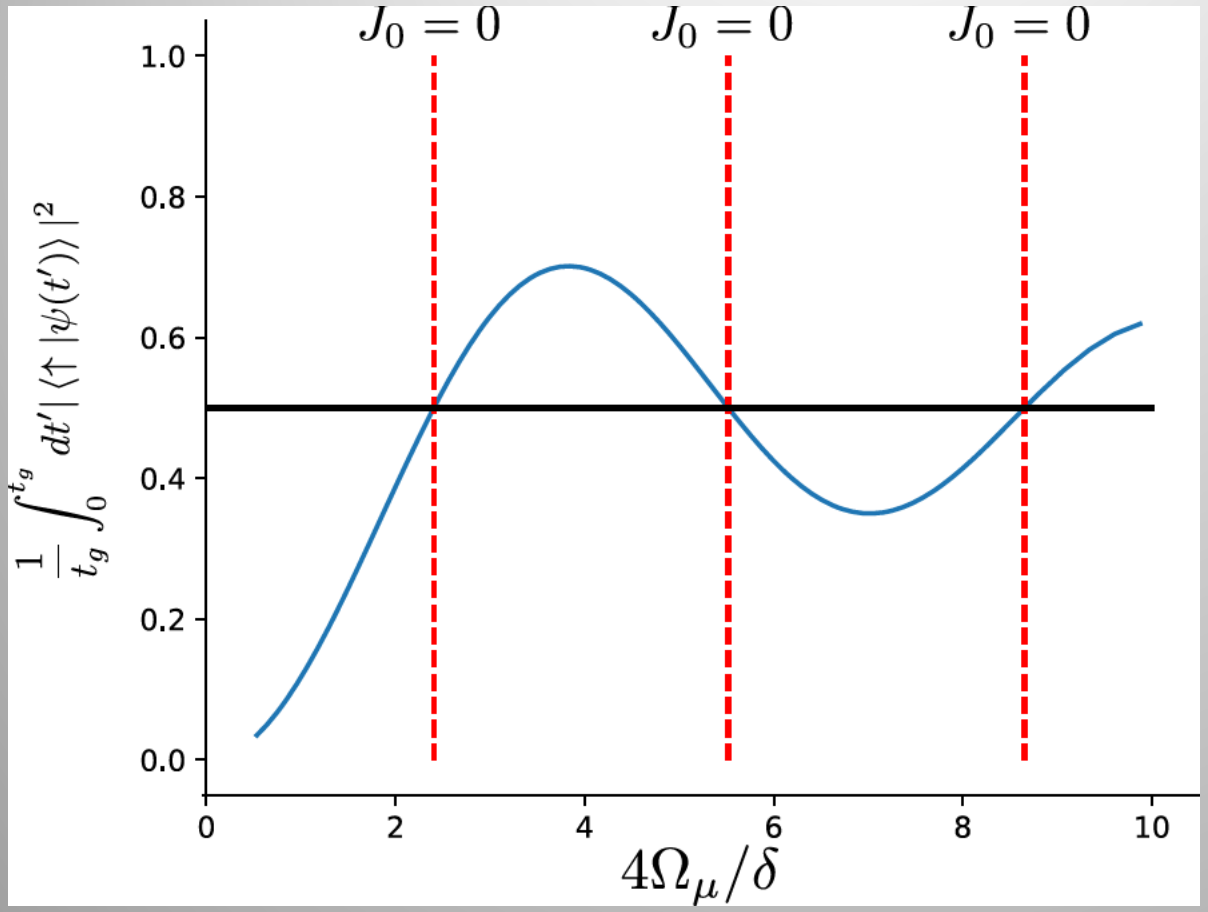

- Time averaged single spin excited state population as a function of tuning.
- Time average is exactly ½ at IDD points.
- Qubit frequency shift error can build up away from IDD points.

Rapid diabatic ion transport is a major challenge for surface traps (single or mixed species - sympathetic cooling 'shepherds' – e.g. ^{9}Be and ^{25}Mg)

Basic Scheme

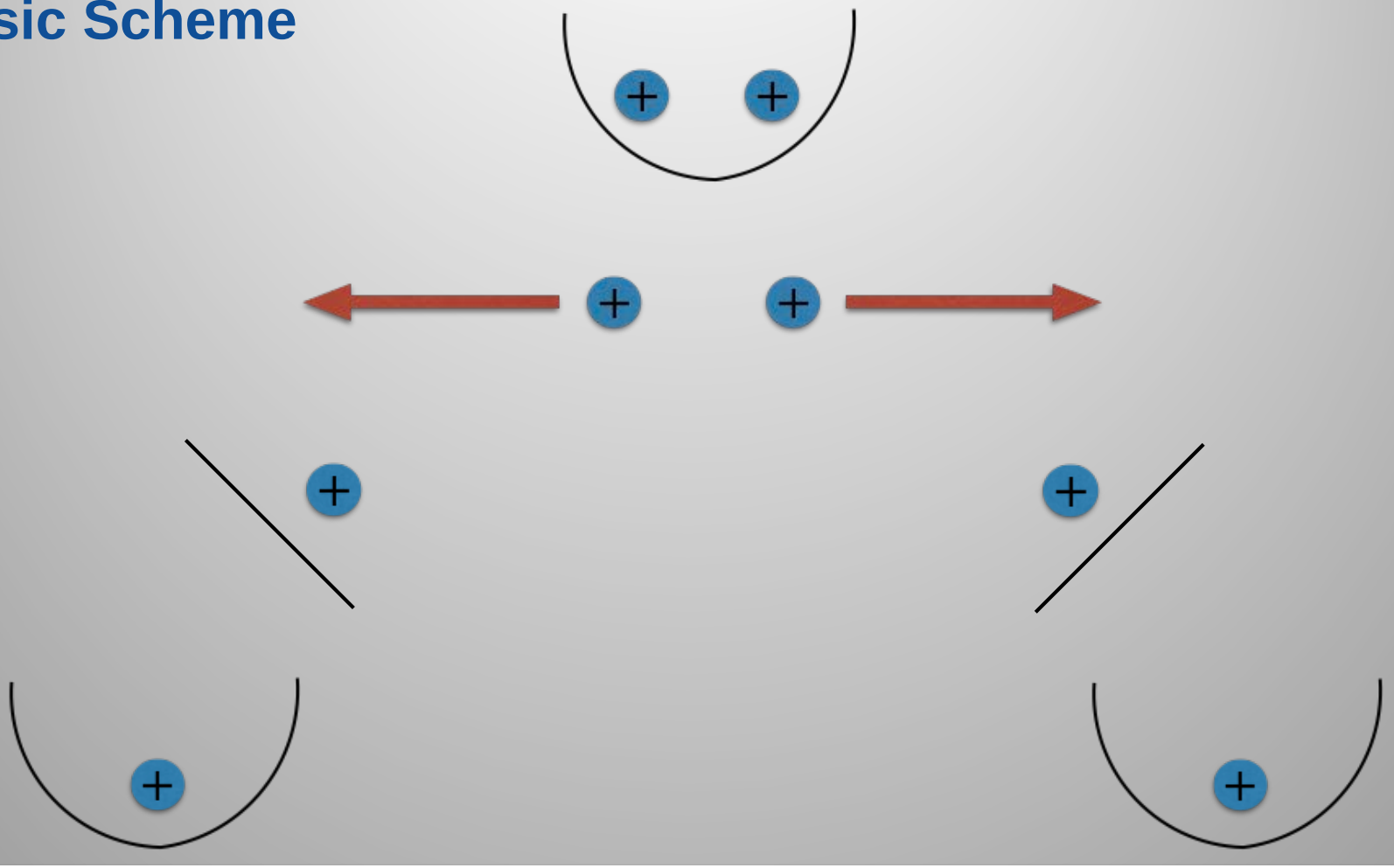

Computational / theory difficulty: need accurate wave-packet evolution over orders of magnitude in length scale. Also wan to control Gaussian spread.

Be/Mg
wavepackets
~ .01 micron

Too many grid points!

‘Noisy’ errors in quantum sensors & computers drive design innovations to minimize their impact – reprise!

- Threshold theorem, quantum error correction, fault tolerance
- Quantification of quantum noise processes and their impact:
  - Ramsey Interferometry Noise – quantum projection & the ‘standard quantum limit’
  - Allan deviation
  - Example: Noise interacting with differing quantum correlation – e.g. squeezing
  - Quantum process tomography / Randomized benchmarking
- Microscopic models of noise processes – Hamiltonians for gate and sensor physics.
  - Control, ‘SPAM,’ and intrinsic (quantum, thermal etc.) noise.
  - Interesting computational challenges often go hand and hand with accurate assessment of noise impacts.
- Noise mitigation for different gate schemes
  - dynamical decoupling, and Molmer-Sorensen gate vs. polychromatic gates with intrinsic dynamical decoupling.
- Case study 1 – Atom interferometry for gravity/gyroscopic sensing.
- Case study 2 – Ion trap quantum computing (physics error budget, ‘magtraps’)

Backups!

Optically stimulated Raman transitions – Rabi oscillations between hyperfine states - advantages for quantum interferometry!

Level scheme

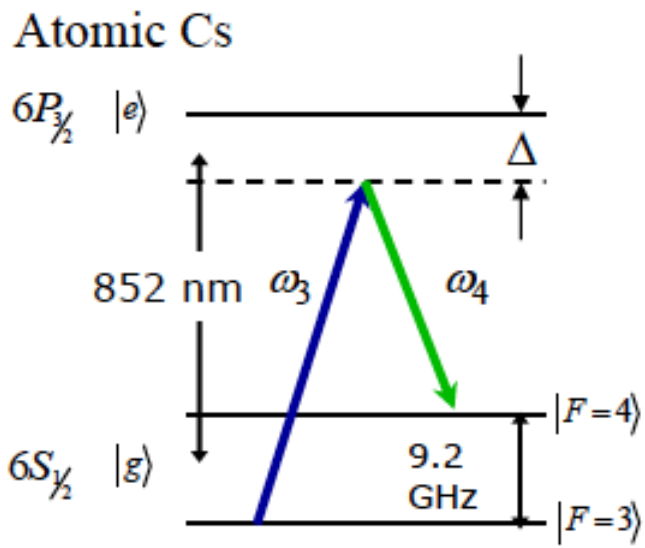

Excitation Geometry

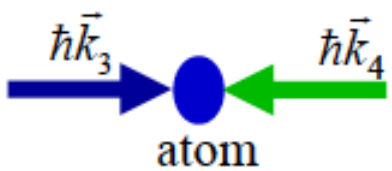

Doppler sensitive configuration

- $\mathbf{k}_3$, $\mathbf{k}_4$ counter-propagate

Ground states

- Avoid spontaneous emission
- Excitation between magnetic field insensitive sublevels

Large detuning D

- Effective 2-level system

  $F=3, m_f=0 \leftrightarrow F=4, m_f=0$

- Effective traveling wave excitation

  $\mathbf{k}_{eff} = \mathbf{k}_3 - \mathbf{k}_4 \sim 2\mathbf{k}_3$

- Effective transition frequency

  $\Delta\omega_{eff} = \omega_3 - \omega_4$

The Mølmer-Sørensen (bichromatic) gate is 'heat resistant!'

- MS-gate effective Rabi frequency is independent of the ion phonon occupation.
- Interference of different orderings of the ion excitation paths is key.
- Geometric phase gates similar (Milburn et. al.)
- Gate speed is an issue (optimality in the presence of differing noise sources)
- Magtraps vs. laser driven traps

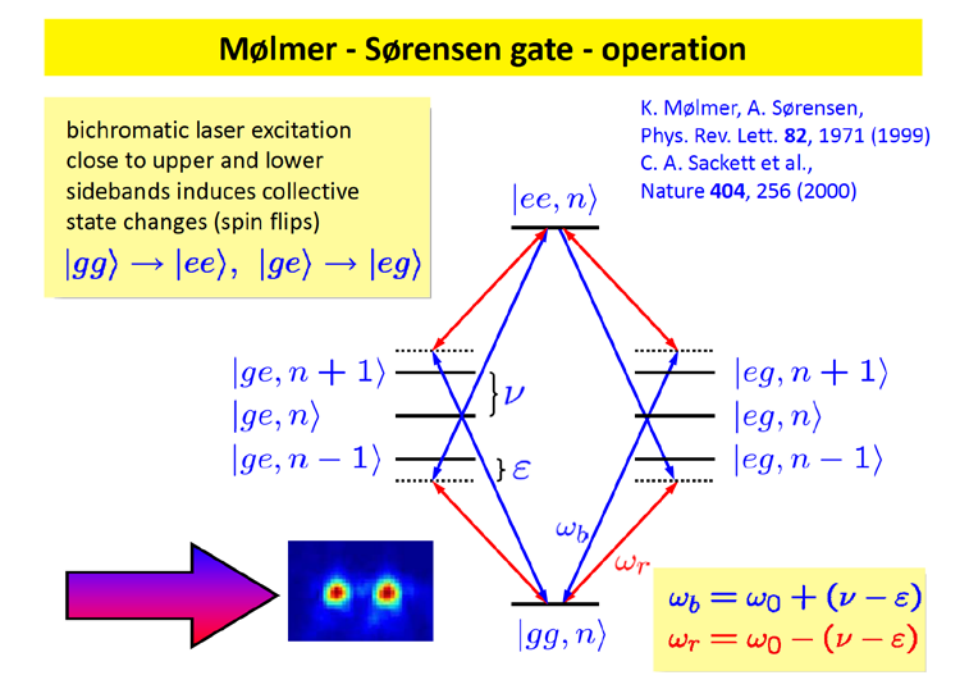

$$\left(\frac{\tilde{\Omega}}{2}\right)^2 = \frac{1}{\hbar^2}\left|\sum_m \frac{\langle een|H_{\text{int}}|m\rangle\langle m|H_{\text{int}}|ggn\rangle}{E_{ggn} + \hbar\omega_i - E_m}\right|^2$$

$$\tilde{\Omega} = -\frac{(\Omega\eta)^2}{2(\nu - \delta)}$$

Geometric phase gates

$$\hat{H}(t) = \hbar\Omega\hat{\sigma}_{x,z}\left(\hat{a}e^{-i\delta t} + \hat{a}^{\dagger}e^{i\delta t}\right)$$

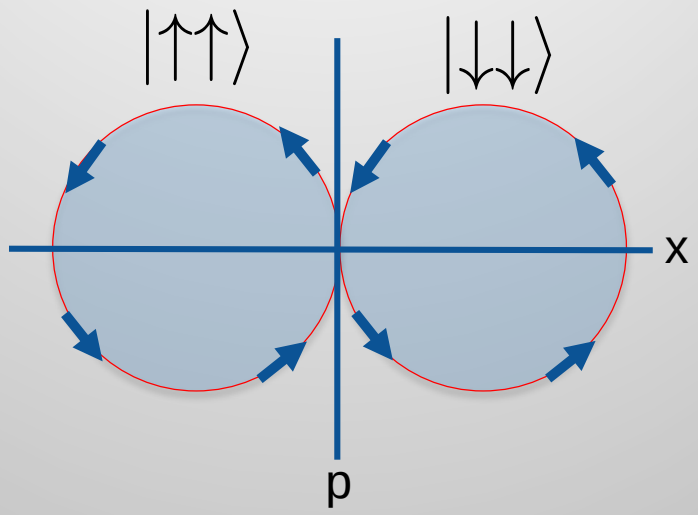

$$|\downarrow\downarrow\rangle \rightarrow e^{i\phi}|\downarrow\downarrow\rangle$$
$$|\uparrow\downarrow\rangle \rightarrow \quad |\uparrow\downarrow\rangle$$
$$|\downarrow\uparrow\rangle \rightarrow \quad |\downarrow\uparrow\rangle$$
$$|\uparrow\uparrow\rangle \rightarrow e^{i\phi}|\uparrow\uparrow\rangle$$

$$\hat{\sigma}_{\alpha} \equiv \hat{\sigma}^1_{\alpha} + \hat{\sigma}^2_{\alpha}$$

PRL **82** 1835 (1999)

Single and two qubit gates with $^{43}Ca^{+}$: (Oxford group – Harty et. al. PRL 113, 220501, 2014 – single qubit)

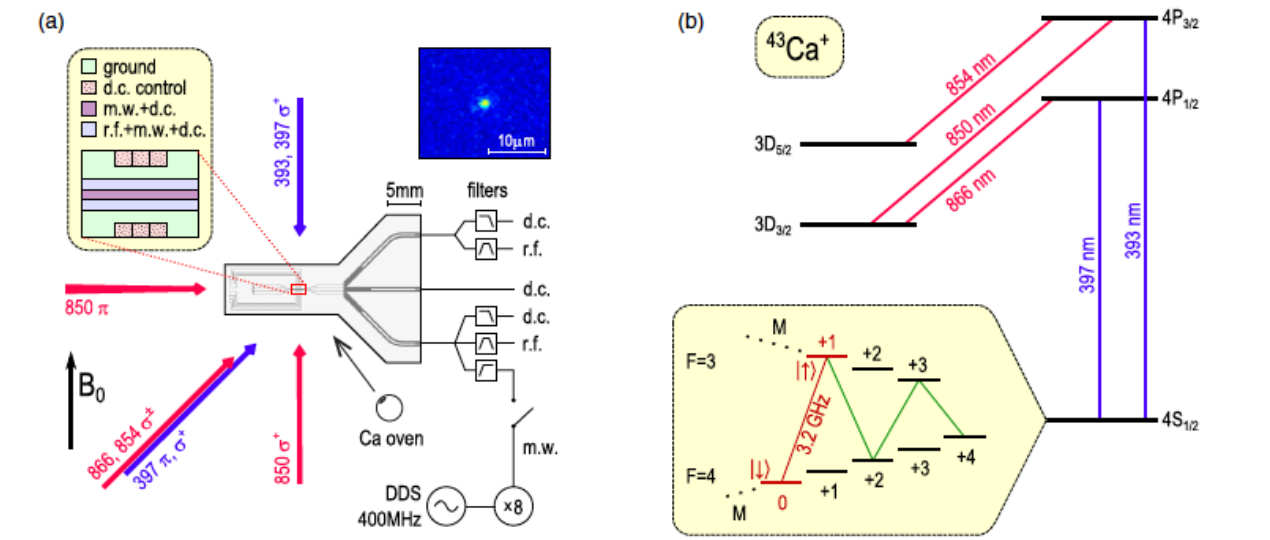

FIG. 1 (color online). The ion trap and the qubit. (a) Schematic diagram of the surface ion trap, showing (left-hand inset) central electrode layout. Microwave (m.w., 3.2 GHz) signals are combined with the trap radio frequency voltage (rf, 40 MHz) via filters, as indicated here for the lower axial electrode. Also shown are laser beam directions and polarizations with respect to the static magnetic field $B_0 = 146$ G. The violet 397 nm Doppler-cooling beam is elliptically polarized such that it contains only π and σ^+ polarizations, and copropagates with linearly ($\sigma^{\pm}$) polarized infrared repumping beams. Circularly σ^+ and linearly π polarized beams are used for state preparation and readout (the π beam is at $\sim 45°$ to the plane of the figure and reflects off the trap surface). To load the trap, neutral Ca atoms effusing from the oven are ionized by laser beams at 423 and 389 nm which copropagate with the Doppler-cooling beams. Ion fluorescence is collected by an imaging system perpendicular to the plane of the trap; the right-hand inset shows an image of a single $^{43}Ca^{+}$ ion, which is trapped 75 μm above the electrodes. (b) $^{43}Ca^{+}$ level structure, showing optical transitions used for Doppler cooling, qubit state preparation, and readout. The inset shows part of the ground level hyperfine structure, labeled by quantum numbers F and M, with the qubit $|\downarrow\rangle$ and $|\uparrow\rangle$ states, the 3.2 GHz qubit transition (red), and the auxiliary transitions (green) used for state preparation and readout. The Zeeman splittings between adjacent M states are ≈ 50 MHz.

- Harty PRL experiment: single 'clock state' qubit with external magnetic field chosen to remove long time sensitivity to magnetic field noise

Ballance et al :: rates for 'stretch' qubit in $^{43}Ca^{+}$

Rabi frequency	$\Omega_{\uparrow\downarrow} = \frac{\sqrt{7}}{12}(b_- r_0 + b_0 r_+) g_r g_b \left[\frac{\omega_f}{\Delta(\Delta-\omega_f)}\right]$
Differential light-shift	$\Delta_{\mathrm{LS}} = \frac{7}{48}(e_+^2 - e_-^2) g^2 \left[\frac{\omega_f}{\Delta(\Delta-\omega_f)}\right]$
Elastic dephasing rate	$\Gamma_{\mathrm{el}} = \frac{49}{576}(e_+^2 + e_-^2)\gamma g^2 \left[\frac{\omega_f}{\Delta(\Delta-\omega_f)}\right]^2$
Light-shift force ($\sigma_\pm \perp \sigma_\pm$)	$\Omega_\downarrow = -\frac{1}{6} g_r g_b \left[\frac{\omega_f}{\Delta(\Delta-\omega_f)}\right]$
	$\Omega_\uparrow = \frac{1}{8} g_r g_b \left[\frac{\omega_f}{\Delta(\Delta-\omega_f)}\right]$
Raman scattering rate with $\sigma_\pm$ light	$\Gamma_{\mathrm{Raman}}^{\downarrow} = \frac{1}{36}\gamma g^2 \left[\frac{\omega_f}{\Delta(\Delta-\omega_f)}\right]^2$
	$\Gamma_{\mathrm{Raman}}^{\uparrow} = \frac{23}{576}\gamma g^2 \left[\frac{\omega_f}{\Delta(\Delta-\omega_f)}\right]^2$
Total scattering rate	$\Gamma_{\mathrm{Total}} = \frac{1}{12}\gamma g^2 \left[\frac{1}{\Delta^2} + \frac{2}{(\Delta-\omega_f)^2}\right]$

Magnetic Field Noise

- **For a hyperfine qubit, and slowly varying (adiabatic) external field noisy variations, use the Breit-Rabi form (J= ½) to compute the induced variations in:** $\omega_{eg}\sigma_z$

$$\Delta E_{F=I\pm 1/2} = -\frac{h\Delta W}{2(2I+1)} + \mu_B g_I m_F B \pm \frac{h\Delta W}{2}\sqrt{1+\frac{2m_F x}{I+1/2}+x^2}$$

$$x \equiv \frac{\mu_B B(g_J - g_I)}{h\Delta W} \qquad \Delta W = A\left(I+\frac{1}{2}\right)$$

where ΔW is the splitting (in units of Hz) between two hyperfine sublevels in the absence of magnetic field B.

- **Stochastic magnetic field variations can also enter through induced state flips with Lindblad operators ~** $\sqrt{B_{eg}}\sigma_{\pm}$

The atomic fountain interferometer is making a stroboscopic movie of falling atoms

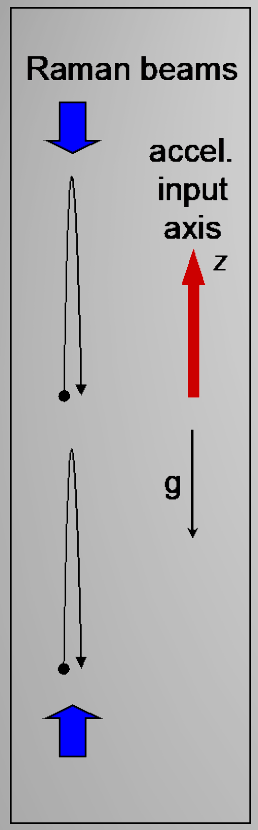

Paired atom fountains 'interrogated' by common Raman lasers – PINS gradiometer

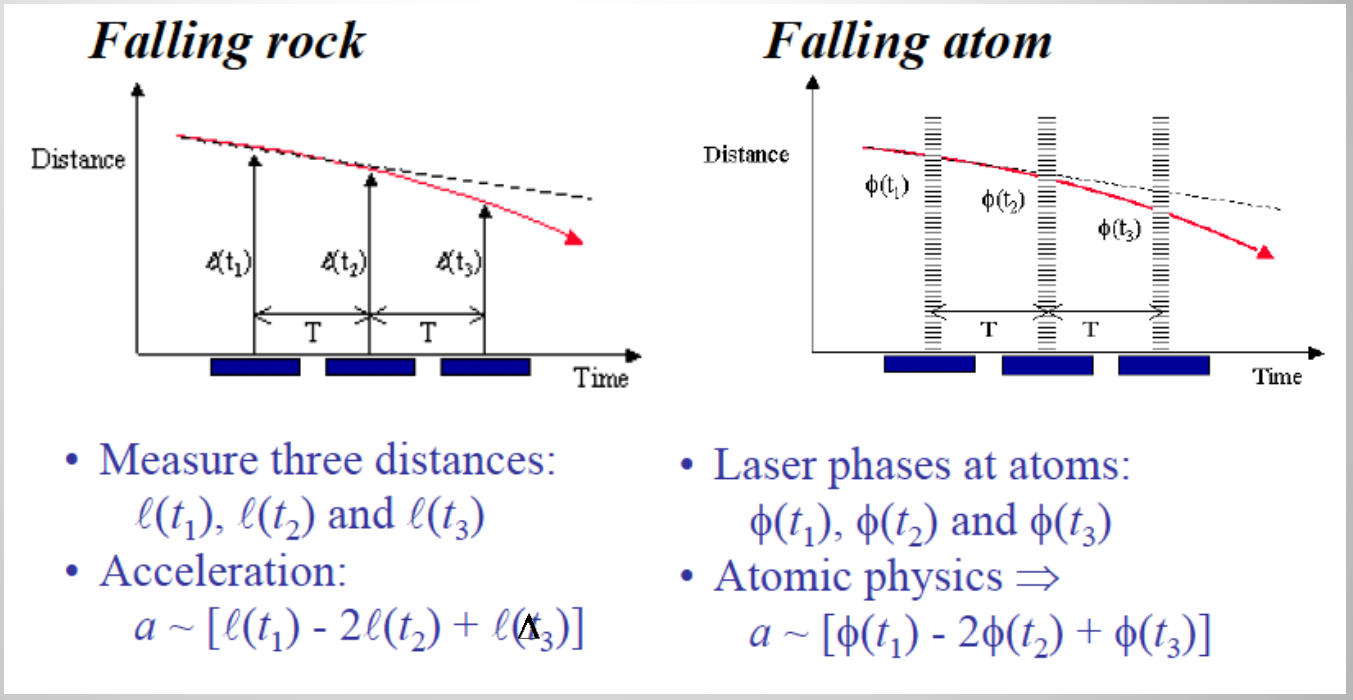

Gravity gradient is $T_{zz} = (g_1-g_2)/L$. 1 Eötvös is 10^{-9} s^{-2}. Gravity gradient of Earth at Earth surface is 3 10^{-6} s^{-2}.

Gravity gradient of 25 kg sphere at 1 meter is 3.4 10^{-9} s^{-2}.

GG directly above 1.5 x 1.5 m^2 tunnel buried 30 m ~ .8 10^{-9} s^{-2}.

Individual interferometer gross phase ~ $k_{eff}\, gT^2$ ~ 10^8 radians (due mainly to the earth). Shot noise limited phase sensitivity ~ $1/\sqrt{N_{pulse}}$ ~ 10^{-3} rad.

Pulsed Atomic Clock

$$|\text{atom}\rangle = |1\rangle$$

beamsplitter

$$\frac{1}{\sqrt{2}}\left(|1\rangle + |2\rangle\right)$$

$$\begin{array}{l} 2 \\ 1 \end{array} \Big\} \Delta E$$

wait time t

$$\frac{1}{\sqrt{2}}\left(|1\rangle + e^{i(\Delta E)t}|2\rangle\right)$$

beamsplitter

$$\frac{1}{2}\left[\underbrace{\left(1 - e^{i(\Delta E)t}\right)}_{N_1}|1\rangle + \underbrace{\left(1 + e^{i(\Delta E)t}\right)}_{N_2}|2\rangle\right]$$

output ports

can measure times $t \sim \frac{1}{\Delta E} \sim 10^{-10}\,\text{s}$

Concept: Two Atomic Clocks

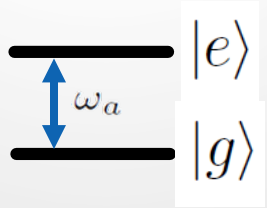

$$\frac{1}{\sqrt{2}}|g\rangle + \frac{1}{\sqrt{2}}|e\rangle$$

$$\frac{1}{\sqrt{2}}|g\rangle + \frac{1}{\sqrt{2}}|e\rangle$$

Time

1. Laser pulses creates superposition of clock states, "starts clock ticking"
2. Second pulse represents end of measurement, phase reflects amount clock ticked during measurement time

Phase evolved by atom after time T (second clock starts slightly later, by amount L/c for baseline length L, than first because of light travel time, but also ends time L/c later)

$$\frac{1}{\sqrt{2}}|g\rangle + \frac{1}{\sqrt{2}}|e\rangle e^{-i\omega_a T}$$

$$\frac{1}{\sqrt{2}}|g\rangle + \frac{1}{\sqrt{2}}|e\rangle e^{-i\omega_a T}$$

Note: in actual measurement, there are more pulses in between first and final pulse

‘Spontaneous’ photon scattering is likely the dominant error source for fast gates.

- Scattering rates required for Lindblad operators (via Uys, 2010, Ballance, 2014, Ozeri et. al.)

$$\Gamma_{\rm el} = \frac{g^2\gamma}{4}\sum_k \left| \sum_{e,q} \frac{\langle\uparrow|\,\hat{\epsilon}_q\cdot\boldsymbol{r}\,|e\rangle\,\langle e|\,b_k\hat{\epsilon}_k\cdot\boldsymbol{r}\,|\uparrow\rangle}{\mu^2\Delta_e} - \frac{\langle\downarrow|\,\hat{\epsilon}_q\cdot\boldsymbol{r}\,|e\rangle\,\langle e|\,b_k\hat{\epsilon}_k\cdot\boldsymbol{r}\,|\downarrow\rangle}{\mu^2\Delta_e} \right|^2$$

- Rayleigh Scattering rate

- Table of Raman drive features: Rabi frequency to scattering…(stretch qubits)

Rabi frequency	$\Omega_{\uparrow\downarrow} = \frac{\sqrt{7}}{12}(b_- r_0 + b_0 r_+) g_r g_b \left[\frac{\omega_f}{\Delta(\Delta-\omega_f)}\right]$
Differential light-shift	$\Delta_{\rm LS} = \frac{7}{48}(e_+^2 - e_-^2) g^2 \left[\frac{\omega_f}{\Delta(\Delta-\omega_f)}\right]$
Elastic dephasing rate	$\Gamma_{\rm el} = \frac{49}{576}(e_+^2 + e_-^2)\gamma g^2 \left[\frac{\omega_f}{\Delta(\Delta-\omega_f)}\right]^2$
Light-shift force ($\sigma_\pm \perp \sigma_\pm$)	$\Omega_\downarrow = -\frac{1}{6} g_r g_b \left[\frac{\omega_f}{\Delta(\Delta-\omega_f)}\right]$
	$\Omega_\uparrow = \frac{1}{8} g_r g_b \left[\frac{\omega_f}{\Delta(\Delta-\omega_f)}\right]$
Raman scattering rate with $\sigma_\pm$ light	$\Gamma^\downarrow_{\rm Raman} = \frac{1}{36}\gamma g^2 \left[\frac{\omega_f}{\Delta(\Delta-\omega_f)}\right]^2$
	$\Gamma^\uparrow_{\rm Raman} = \frac{23}{576}\gamma g^2 \left[\frac{\omega_f}{\Delta(\Delta-\omega_f)}\right]^2$
Total scattering rate	$\Gamma_{\rm Total} = \frac{1}{12}\gamma g^2 \left[\frac{1}{\Delta^2} + \frac{2}{(\Delta-\omega_f)^2}\right]$

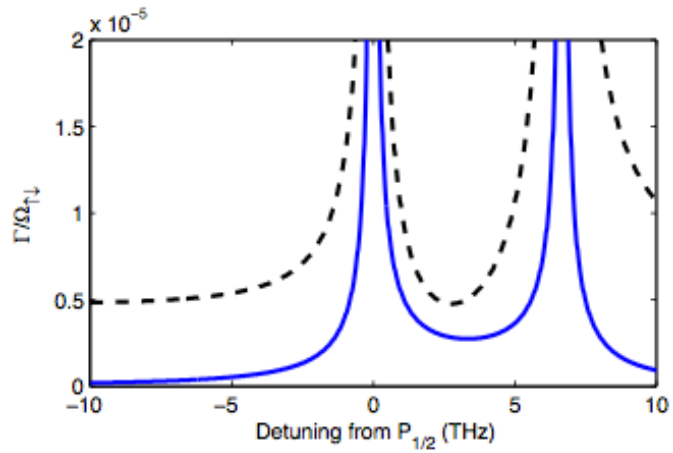

Figure 3.3: Ratio of the scattering rates to the Raman Rabi frequency, evaluated for the stretch states. The solid blue line is calculated using the rate of Raman scattering alone, and the dashed black line using the total scattering rate (Raman+Rayleigh).